Development of MEMS-Based Piezoelectric Microvalve Technologies

Eui-Hyeok Yang[*,**], Choonsup Lee and J. M. Khodadadi[1]

Jet Propulsion Laboratory, California Institute of Technology,
4800 Oak Grove Drive, Pasadena, CA 91109, USA
[1]Mechanical Engineering Department, Auburn University,
270 Ross Hall, Auburn, AL 36849-5341, USA

In this paper, we describe an overview of our development of piezoelectric microvalves for microspacecraft applications, and a summary of the results of the computational modeling of the microvalves. The microvalves have been designed, fabricated and characterized for the proportional flow control of propellant for spacecraft micropropulsion. The microvalve consists of a custom-designed piezoelectric stack actuator bonded onto silicon valve components with the entire assembly contained within a metal housing. The valve seat configuration includes narrow-edge seating rings and tensile-stressed silicon tethers that enable the normally closed and leak-tight operation. A concentric series of narrow rings simulates a "knife-edge" seal by greatly reducing the valve contact area, thereby increasing the seating pressure and consequently reducing leakage. Leak testing of the microvalve, conducted using a Helium leak detector, showed a leak rate of approximately 5×10^{-3} sccm at 800 psi for the gas-compatible version and a leak rate of approximately 3×10^{-6} scc/s at 50 psi for the liquid-compatible version, respectively. Dynamic microvalve operations (switching rates of up to 1 kHz) have also been successfully demonstrated. The measured static flow rate for the gas-compatible microvalve under an applied potential of 10 V was 52 sccm at an inlet pressure of 300 psi. The measured forward flow rate for deionized (DI) water for the liquid-compatible microvalve is approximately 64 mg/min at an inlet pressure of 20 psi and an applied voltage of 50 V. The measured power consumption, in the fully open state, was 3 mW at an applied potential of 30 V. The measured dynamic power consumption was 180 mW for 100 Hz continuous operation at 100 psi. A computational fluid dynamics (CFD) package was used for the 3-dimensional modeling of the flow in the liquid microvalve. The liquid experienced the greatest pressure loss as it moved over the rings in the gap between the seat and boss plates. A correlation for the pressure drop coefficient as a function of the gap spacing between the

*Corresponding author, e-mail address: eyang@stevens.edu
**Dr. Eui-Hyeok Yang has transferred to Stevens Institute of Technology, Castle Point on Hudson, Hoboken, NJ 07030, USA

seat and boss plate was obtained. As for the gaseous microvalve, a 1-dimensional compressible flow model was developed, accounting for the excessive frictional effects of the seat rings. The variations of compressible flow quantities due to friction were studied, showing the drastic increase in density and static pressure in contrast to a rather small increase in the Mach number. Also of great importance, the total pressure drop was shown to be significant across the seat rings.

1.   Introduction

Miniaturized, micro/nano spacecraft concepts are of great interest in the aerospace community. Any reduction in the mass and size of a space instrument or subsystem results in nearly exponential savings in launch costs as well as significant increases in mission duration. In order to enable the construction of such 'microspacecraft,' each subsystem will have to be reduced in size and adapted in function to fit within the spacecraft size and mass envelope, and thereby require extensive miniaturization. Furthermore, thrust levels and impulse bits will have to be reduced in magnitude. The reduction in thrust levels and impulse bits requires fine control of very small propellant flow rates. Microvalves are needed to control these propellant flows. Given the severely limited power constraints of the overall micropropulsion system, microvalves with "normally closed" operation are needed in order to consume power only during the opening or closing process. Solenoid valves have been refined by decades of technology development, but they suffer from fundamental limitations such as volume and power consumption. Many turns of copper wire with a volume of a high-permeability core material are required to generate a high actuation force, making the actuator larger and heavier than desired for many applications. Although significant progress has been made in the miniaturization of solenoid valves, these miniaturized valves require further improvement in performance for the valve actuation time[1–7] or seating force.[8–12] Slow valve actuation leads to long thruster on-times and large impulse bits. An alternative, thermally actuated valve technology suffers from the risk of un-commanded valve opening due to changes in the environment, i.e., ambient heating or cooling resulting in uncontrolled initiation of the actuation mechanism. The gas and liquid compatible microvalves were required in response to the requirements for a JPL-initiated development of 1-kg-class microspacecraft test platforms. These microspacecraft need leak-tight, low-power microvalves. Due to the microspacecraft's severely limited propellant and power resources, it was critical that the microvalves exhibit leak-tight and low-power operation. Previously developed liquid-compatible microvalves using either electromagnetic or thermal actuators were found to have high power consumption.[13,14] Alternatively, other liquid-compatible microvalves using either electrostatic or piezoelectric actuators did not meet the demanding requirements for low leak rates.[15,16] Therefore, we have developed the microvalve meeting the requisite performance requirements, and experimentally demonstrated and modeled the microvalve operation.[17,18] Extremely low leak rates of 5×10^{-3} sccm were demonstrated for an inlet pressure of 800 psi. In this paper,

we provide an overview of the successful development of leak-tight, low-power, fast-actuation microvalves for proportional flow control of gas and liquid propellants. Also, we discuss the results of the recent computational modeling studies of the flow properties within the liquid and gaseous microvalves.

2. Microvalve Design

2.1 *Gas-compatible microvalve*

The core components of a piezoelectric microvalve described in this paper are a seat plate, a boss plate and an actuator as shown in Fig. 1. The microvalve components for handling high-pressure gas-propellants avoid the use of fragile membranes in order to allow high-pressure operation. Major elements of the microvalve design include the custom designed piezoelectric stack actuator and the seating configuration consisting of narrow seat rings. The custom-designed stack of piezoelectric actuators consists of peripheral active zones and an inactive central zone. The active zones are mechanically separated (by deep U-grooves) from the central, inactive zone. These zones are bonded to corresponding peripheral and central areas of the boss plate. Application of a voltage (~60 V) to the piezoelectric stack causes the active zones to vertically expand by 5 μm, lifting the boss center plate (bonded to the inactive zone), away from the seat plate. This actuation creates a channel between the two seating surfaces, permitting the passage of fluids as shown in Fig. 2. Since the piezoelectric actuator is essentially a stacked capacitor, it consumes extremely low power when it is not moving, thus allowing a near zero-power,
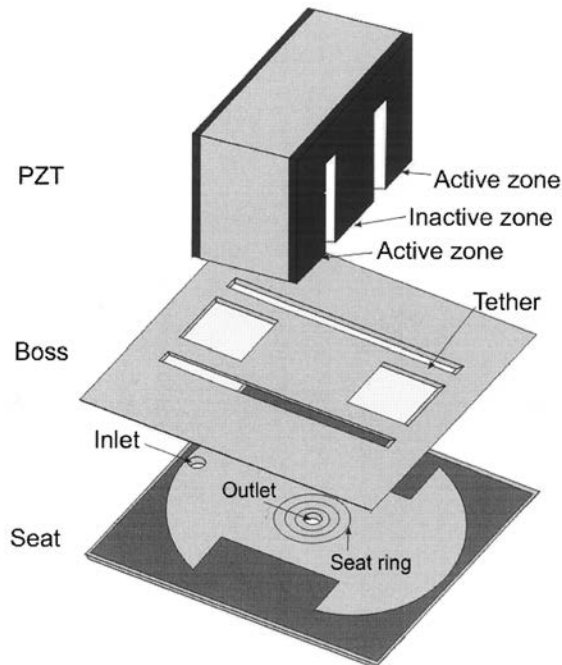

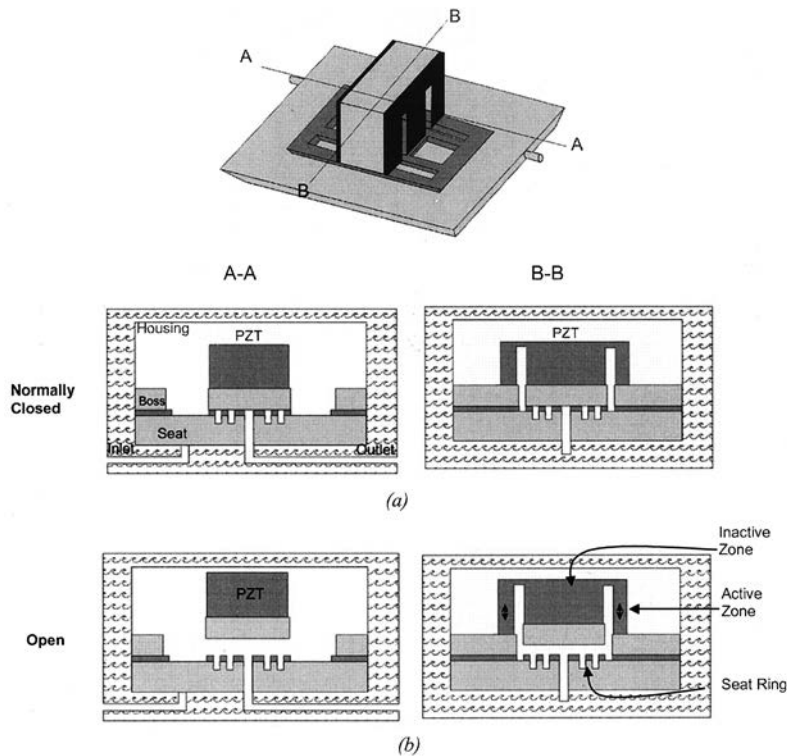Fig. 1.   Schematic of the gas-compatible piezoelectric microvalve.

Fig. 2.   Operating principle of the gas-compatible microvalve. Applying a voltage (~60 V) to the piezoelectric stack makes the active zones dilate by 5 μm, lifting the center boss plate (bonded to the inactive zone of the stack) away from the seat plate. Thus, a channel is created between the two plate surfaces, allowing for the passage of fluids. (a) Microvalve closed; (b) microvalve opened.

open or closed operation for the microvalve. A concentric series of narrow rings on the seat plate (10 rings total) is designed to provide the redundancy necessary to maintain a leak-tight operation in the event of damage to individual seating rings.   The narrow rings (1.5 μm wide and 10 μm deep) simulate a "knife-edge" seal by reducing the contact area, thereby increasing the seating pressure and consequently reducing internal leaks. The center portion of the boss plate has a 2 μm thick silicon dioxide layer functioning as a hard seat coating material. The boss plate is bonded to the seat plate via metal-to-metal compression along the periphery. The thickness of the silicon dioxide coating on the boss plate varies, being slightly thicker (2 μm) in the center than at the periphery. This oxide thickness difference results in the generation of tensile stress in the silicon tether suspension. The tensile stressed silicon tether suspension of the boss plate provides an initial valve-seating pressure. The dominant seating pressure is, in fact, applied by the piezoelectric actuator during the as-closed-state of the microvalve. This seating pressure is achieved using the following fabrication and assembly procedure: A voltage of 10 V is applied

initially to the piezoelectric stack actuator during bonding onto the boss plate. Once bonded, this assembly procedure insures that the boss plate is pressed onto the seat plate by the inactive zone (attached to the boss center plate) of the piezoelectric stack prior to the microvalve operation.

2.2 *Gas and liquid-compatible microvalve*

The microvalve compatible with both gas and liquid propellants is also actuated using a custom-designed piezoelectric stack actuator, which is bonded onto silicon-based components consisting of a valve seat, a lower boss, and an upper boss, as shown in Fig. 3. The microvalve described in this section has a silicon membrane called the upper-boss, for isolating the piezoelectric actuator from the liquid effluent. Because the liquid effluent remains inside the silicon chamber, it does not cause an electrical short within the piezoelectric actuator. The upper boss layer is compression bonded to the lower boss. The bonded boss stack is subsequently bonded to the valve seat. Finally, the custom-designed piezoelectric actuator is epoxy bonded to the top of the upper boss layer. The operation principle is similar to that of the gas-compatible microvalve. The segmented piezoelectric stack actuator consists of two "actuation" zones surrounding a central inactive zone. Figure 4 shows the microvalve operation principle. The microvalve is in the normally closed ("off" state), as shown in Fig. 4(a). The normally closed condition is achieved by applying an initial seating pressure on the valve seat during the bonding of the piezoelectric
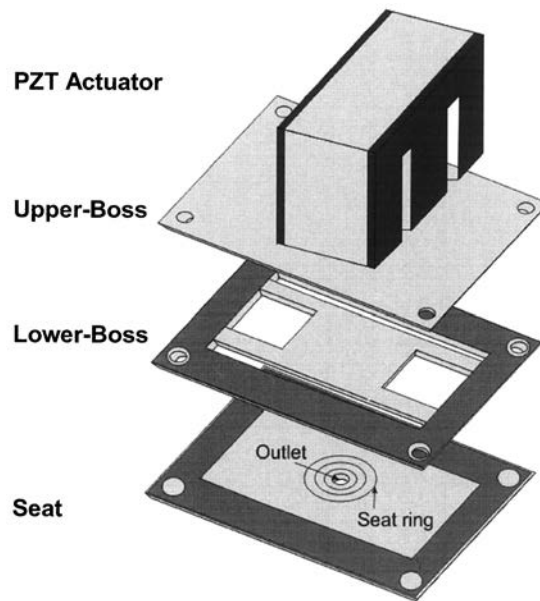

Fig. 3. Schematic of the liquid-compatible microvalve. All silicon components are metal-to-metal thermocompression bonded and the custom-designed piezoelectric stack is bonded on top of the upper-boss wafer.
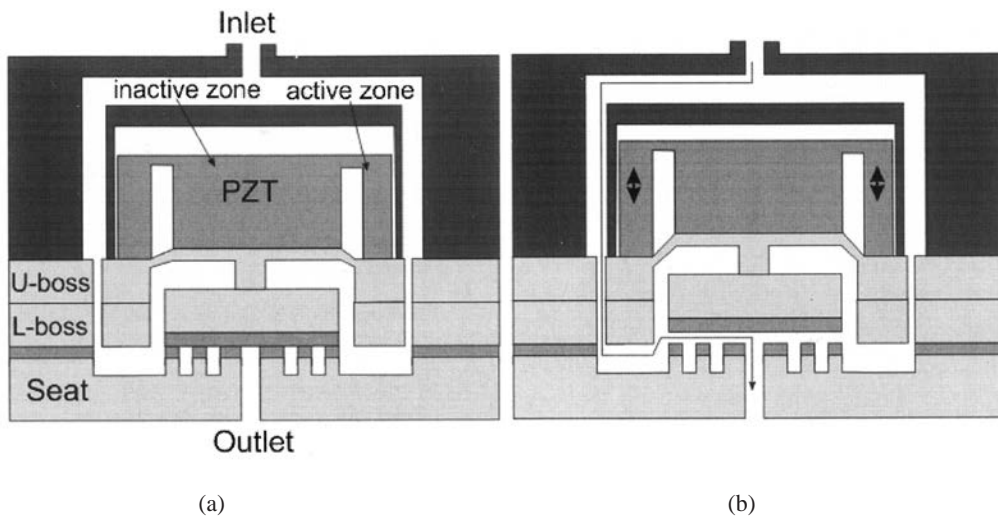
Fig. 4.   Operating principle of the liquid-compatible microvalve. (a) normally-closed "off" state (b) actuated "on" state.

actuator to the silicon assembly. Application of a voltage to the piezoelectric actuator makes the active zones of the piezoelectric actuator expand vertically, lifting the lower-boss center plate up from the valve seat, as shown in Fig. 4(b). This action opens up a flow path between the inlet and outlet ports. Proportional flow control of the fluid is achieved by controlling the extent of the upward displacement of the piezoelectric actuator by changing the applied voltage.

3.   Fabrication of the Microvalve

3.1 *Gas-compatible microvalve*

   The silicon components of the microvalve are fabricated primarily by deep trench etching (reactive ion etching), deposition, and patterning processes.   All silicon wafers (300 µm thick) for the valve seat and boss plates are thermally oxidized (0.5 µm). The seating rings are first lithographically defined on the valve seat wafer. The silicon dioxide layer is selectively removed in 10:1 buffered oxide etchant (BOE) for 10 min. The wafer is then etched using deep reactive ion etcher (DRIE), in order to generate 10 µm deep seating ring structures. Next, the seat wafer is metallized with Cr/Pt/Au (0.03 µm/0.06 µm/ 0.25 µm) and patterned to define the bonding surfaces. The seat wafer is then subsequently etched from the backside using DRIE, in order to open up vias for the inlet and outlet ports. Figure 5 shows a scanning electron micrograph (SEM) of the seat area of a microvalve. A 2-µm thick silicon dioxide is grown by plasma enhanced chemical vapor deposition (PECVD) and patterned on the boss wafer. The oxide layer is etched in BOE (10:1) for 40 min. The bonding metals (Cr/Pt/Au) are deposited subsequently and patterned on the periphery of the boss plate.   The boss wafer is then patterned to define the boss (or valve
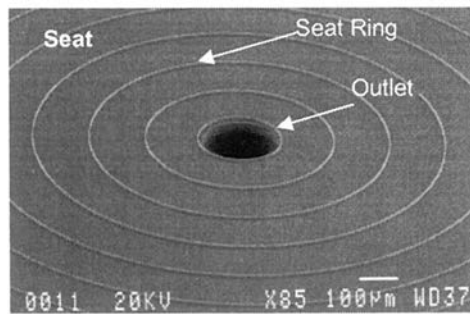
Fig. 5.   Scanning electron micrograph (SEM) image of the seat plate of the high-pressure microvalve. The top surfaces of the seat rings are covered with a 0.5-μm thick thermal oxide.

flap and tethers), which is released in a final DRIE process. The boss and seat wafers are bonded to create a sealed, yet movable structure. An Electronic Visions aligner and thermo-compression bonder is used to align and bond the two wafers. Then, the piezoelectric stack actuator is carefully aligned (using a specially designed jig) and bonded onto the center top of the boss plate using an epoxy (Hysol E/A 9394, cured at room temperature). Finally, the microfabricated valve components are bonded to stainless steel fixtures, which are then hermetically sealed using the same epoxy.

3.2 *Liquid-compatible microvalve*

Silicon wafer (300 μm thick) used for the valve seat plate is thermally oxidized (0.5 μm oxide). The seating rings are first lithographically defined on the valve seat wafer. The silicon dioxide layer is then selectively removed in a 10:1 BOE. The remaining oxide forms the masking layer for DRIE, in order to generate 10 μm deep seating ring structures. Following the metallization step, a central outlet port is formed using DRIE. Fabrication of the lower boss plate is initiated by growing and subsequently patterning a 2-μm thick PECVD silicon dioxide layer. Once again, the oxide layer is etched in BOE (10:1). Also, as in the previous case, the bonding metals (Cr/Pt/Au) are formed. The boss wafer is then patterned to define the boss (or valve flap and tethers), which is released in a final DRIE process.   On the upper boss plate, the 150 μm thick silicon membrane is defined using DRIE, followed by the deposition and patterning of the Cr/Pt/Au bonding layer. Four inlet ports are formed subsequently in each corner of the boss plate using DRIE. The upper boss, lower boss and seat wafers are bonded simultaneously to create a sealed, yet movable structure. Subsequently, the piezoelectric stack actuator is carefully centered (using a specially designed jig) and bonded onto the top of the boss plate using an epoxy (Hysol E/A 9394, cured at room temperature). Finally, the microfabricated valve components are bonded to stainless steel fixtures, which are then hermetically sealed using the same epoxy. Figure 6 shows the fully assembled and packaged microvalve, compatible with liquid propellants. Of course, this microvalve is also compatible with gas-propellants. The inlet gas tube is then connected to the inlet ports in the upper boss plate. Also seen are the outlet port (diameter: 200 μm) in the seat wafer and the wires for applying voltage to the piezoelectric actuator.
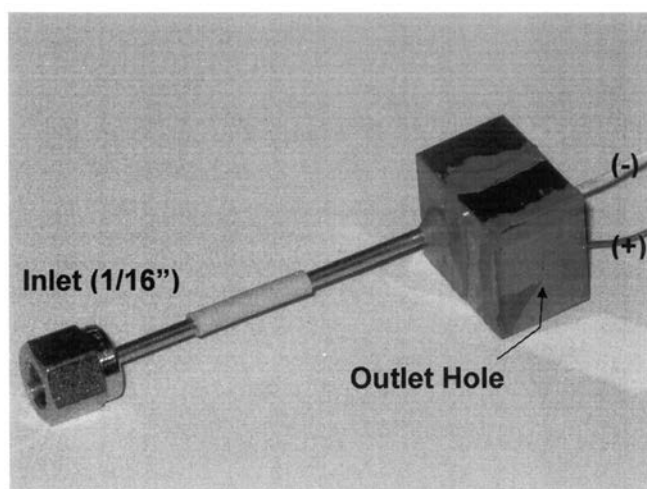
Fig. 6.   Fully assembled and packaged liquid-compatible microvalve.

4.   Characterization

The fully assembled gas-compatible microvalves were tested under inlet pressures of up to 1000 psi. Testing of the microvalve at higher pressures was not possible because 1000 psi is the safety limit of our current test setup. A helium (He) gas based test apparatus was used for the leak and flow testing of the microvalves. Leak testing of a gas-compatible microvalve using a helium leak detector showed an extremely low leak rate of 5×10^{-3} sccm at an inlet pressure of 800 psi. Figure 7 shows the leak rates of three tested-microvalves for inlet pressures between 300 psi and 900 psi. The high seating pressure generated by the piezoelectric stack actuator is responsible for the extremely low leak rates. The static forward flow rates were measured for an actuated microvalve for various actuation voltages and inlet pressures. Measured flow rates, at an actuation voltage of 10 V, are approximately 52 sccm at an inlet pressure of 300 psi.

Leak rate (off state) and flow rate (on state) testing of liquid-compatible microvalves were conducted using Helium-gas and deionized (DI) water, respectively. Helium leak rates were measured using a Helium leak detector. The measured leak rates of several microvalves ranged from 3×10^{-6} scc/s to 4×10^{-5} scc/s at an inlet pressure of 50 psi. For the liquid flow rate measurement, we measured the mass of the DI water flowing out from the valve for a fixed period.   The measured forward flow rates at various inlet pressures for deionized DI water are shown in Fig. 8.[18] As the voltage applied to the piezoelectric actuator increases, the vertical deflection also increases. The increased deflection increases the flow of the DI water, thereby providing proportional flow control operation. The measured flow rate is approximately 60 mg/min at an inlet pressure of 20 psi (for an applied voltage of 40 V). We also measured the DI water flow rate versus the various duty
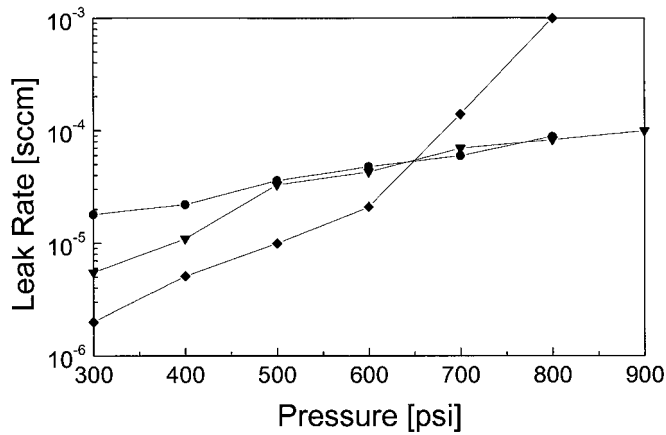
Fig. 7.   Measured internal leak rates for three fabricated normally-closed (non-actuated) microvalve at the pressure range of 300–800 psi. The leak rate at the lower pressure regime is found in the ref. 17.
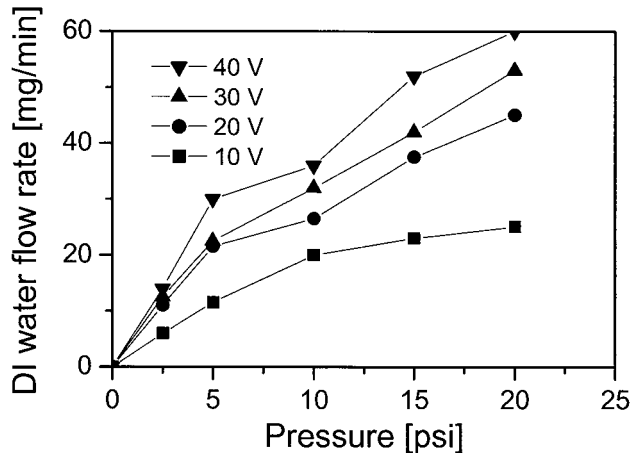

Fig. 8.   Measured flow rates for an actuated, liquid-compatible microvalve at various inlet pressures. As the voltage applied to the piezoelectric actuator increases, the vertical deflection increases. This action increases the flow of the DI water, thereby providing the proportional flow control. The measured flow rate is approximately 60 mg/min at an inlet pressure of 20 psi (for an applied voltage of 40 V).[18]

ratios of the pulsed voltage signal for different inlet pressures. The measured dynamic flow rate is 30 mg/min at a 90% pulse width for a 15 psi inlet pressure.

After the series of flow tests described above, a cycling test was performed for 10^5 cycles using a gas-compatible microvalve. The microvalve was connected to a Helium gas

tank regulated at 100 psi, and was actuated with an applied 1 Hz, 10 V square wave. After 10^5 cycles operation, the leak rates were measured again. No significant degradation was observed in the leak rate in the as-closed state.

Piezoelectric valves offer significant advantages over solenoid-actuated valves for proportional flow control. In general, solenoid valves require operation in a pulse width modulation mode in order to provide the necessary proportional flow control. Piezoelectric microvalves, on the other hand, do not require pulse width modulation because the actuation is directly proportional to the applied voltage.   Since the power consumption of a static piezoelectric actuator is negligible, nearly zero-power microvalve operation is possible during the firing of microthrusters. The measured static (DC) power consumption required to keep the microvalve fully open is about 3 mW at 30 V. This static power consumption is primarily due to leakage currents in the piezoelectric stack. The dynamic (AC) power consumption of the piezoelectric microvalve, resulting from dissipation during charging and discharging the stacked capacitor, is approximately 180 mW at 100 Hz. We have measured the mechanical resonance frequency of the piezoelectric actuator bonded to silicon microvalve using a laser doppler vibrometer. The measured value is approximately 11.1 kHz, which shows that the microvalve has sufficient bandwidth for providing fast transient response.

5.   Computational Modeling

Detailed information on the local fluid properties and flow-related quantities within microvalves can be obtained through application of the advanced CFD tools. Despite the ongoing refinement of these tools, various difficulties have to be dealt with. For instance, gaseous flows in microvalves can exhibit strong compressibility effects within the low Reynolds-number regime. For liquid flows, such problems are not encountered. Modeling the movement of the various boundaries in response to or because of fluid flow within piezoelectrically-actuated microvalves also offers another computational difficulty. Also, depending on the regime of operation, non-continuum effects for gases have to be accounted for. In this section, summary of results of 3-dimensional (3-D) flow in liquid-compatible microvalves and 1-dimensional compressible flow in gas-compatible microvalves are presented. Only the static operations of microvalves are considered in the modeling.

5.1 *Problem formulation for the liquid microvalve model*

A 3-D structured mesh with 330,000 hexahedral cells that represents the major features of the liquid-compatible microvalve was generated. Due to the symmetry of the microvalve about two planes, only a one-quarter section of the microvalve was modeled. There are twelve concentric thin seat rings positioned at different radii that surround the outlet hole. The width and height of the rings are 1 and 10 µm, respectively. The diameter of the innermost ring is 110 µm and the remaining rings are evenly spaced 150 µm apart. The mesh is denser in regions that experience excessive pressure drop (i.e., between the boss and seat plates and where the flow enters the microvalve). An isometric view of the computational mesh in the vicinity of one of the rings is shown in Fig. 9. The spacing between the lower boss plate and the seat plate ranges from 11 to 13.5 µm (i.e., the distance
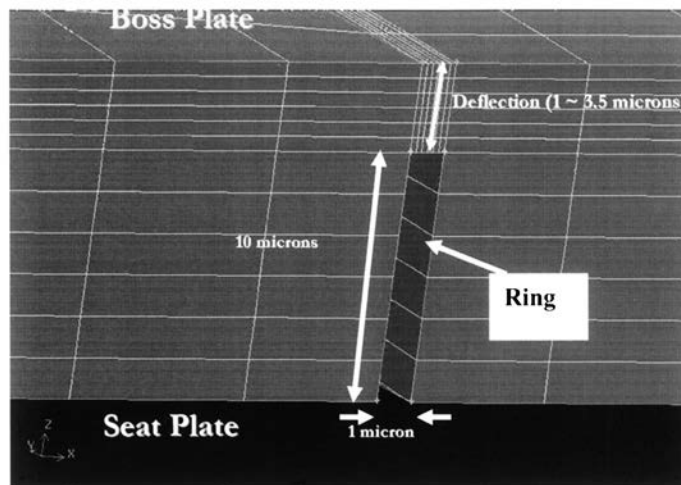
Fig. 9.   Isometric view of a portion of the computational mesh in the vicinity of a ring. The distance between the boss and seat plates in relation to the height of the ring and the gap is clearly shown.

between the top of the valve seat rings and lower boss plate is 1–3.5 μm). The flow is laminar, incompressible, and steady. The governing equations of continuity and momentum in index notation form are:

$$\frac{\partial u_i}{\partial x_i} = 0 \tag{1}$$

$$\frac{\partial}{\partial x_j}\left(\rho u_i u_j\right) = -\frac{\partial p}{\partial x_i} + \mu \frac{\partial}{\partial x_j}\left(\frac{\partial u_i}{\partial x_j} + \frac{\partial u_j}{\partial x_i}\right) \tag{2}$$

Version 6.2 of the commercial CFD code FLUENT was utilized for solving the governing equations. The no-slip boundary condition was chosen for the walls whereas symmetry boundary condition was used on the planes of symmetry. A second-order upwind scheme was chosen to discretize the momentum equation whereas the SIMPLE[19] algorithm was used to couple the pressure (p) and velocities (u_i's). A total of 15 cases were run for three different gaps (i.e., gap spacing values between the bottom surface of the boss-center-plate and the top surface of the seat rings) of 1, 2.7 and 3.5 μm and 5 inlet stagnation pressures of 3, 5, 10, 15 and 20 psig with water as the working fluid. The Reynolds numbers based on the outlet tube diameter for different cases are reported in Table 1. The experimental mass flow rates (Fig. 8) were used to calculate the mean velocity at the outlet of the microvalve. The Reynolds number varies from 0.63 to 6.35.

Table   1
The Reynolds number at the outlet port of the microvalve for various deflections at different total pressures.

Applied Voltage (V)	Deflection (microns)	$\Delta P_t = P_{t\,inlet} - P_{t\,outlet}$				
		3 psig	5 psig	10 psig	15 psig	20 psig
10	1	0.63	1.27	2.12	2.54	2.86
20	2	1.16	2.33	2.96	4.23	4.87
30	2.7	1.48	2.54	3.60	4.97	5.71
40	3.5	1.69	3.17	3.91	5.61	6.35

5.2 *Results of the liquid microvalve modeling study*

The pathlines of flow (tracked by imaginary particles) are shown in Fig. 10 for the case of 2.7-μm-gap and a pressure drop of 2.4 psi. The monitored particles are released at the inlet plane from two rakes placed normal to each other.   The monitored "pathlines" are colored by the local stagnation pressure values. Pressure is almost constant within the inlet tube but drops suddenly and markedly where the flow impacts the valve seat plate that is located 10 μm away from the inlet port. Once the flow emerges into the microvalve cavity, pressure remains almost constant. Within the big cavity of the microvalve, the fluid particles prefer to flow over the tether rather than beneath it due to lower resistance. Once the flow passes over the rings in the gap between the seat and the boss plates, its pressure monotonically decreases (Fig. 11). Since most of the pressure drop occurs across the rings, especially for small deflections, a 2-D axisymmetric analysis limited to the flow over the rings was also performed.[20] Pressure drop over the rings determined from the 2-D analysis verified the accuracy of the 3-D results, which are consistently lower than the 2-D predictions.[18] The dependence of the pressure drop coefficient (K) as a function of gap is shown in Fig. 12. Since the pressure drop changes linearly with respect to change in mass flowrate,[18] the value of K for a given gap is constant. The empirical dependence obtained by plotting a trendline through the points in Fig. 12 is given by:

$$K = \frac{\Delta P_t}{\dot{m}} = 188.29 e^{-1.3 \times def} \tag{3}$$

where *def* is the value of gap in microns, ΔP_t is the pressure drop (the difference between the inlet and outlet stagnation pressures) in *psi* and $\dot{m}$ is the mass flowrate of the system in mg/s.

5.3 *Modeling of the gaseous compressible flow*

One-dimensional modeling of frictional compressible gaseous flow through the gas-compatible microvalve has also been studied.[21] Focusing on the gap between the boss and seat plates, variations of flow properties, namely the Mach number, velocity, pressure, temperature, density, total pressure and entropy, were predicted using a 1-D radial flow model. The radial flow model was developed for steady, axisymmetric, compressible flow
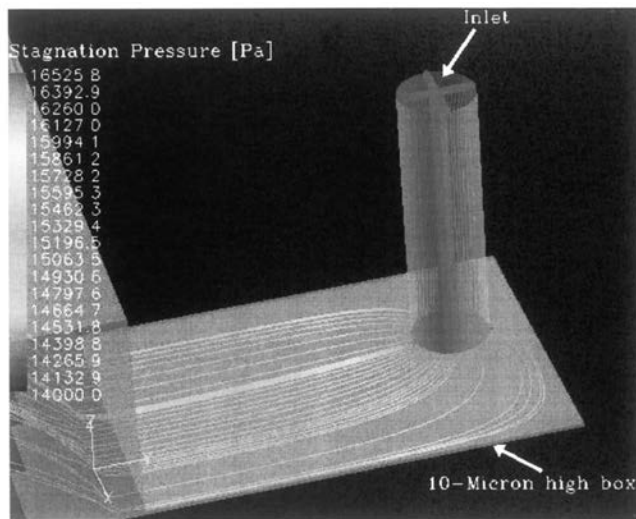
Fig. 10. Isometric view showing pathlines of selected particles within the inlet plane for a gap of 2.7 mm and pressure drop of 2.4 psi. The path of particles released at the inlet are colored by the local fluid stagnation pressure. The color bar on the left shows the pressure values. The particles finally emerge into the main cavity of the microvalve.
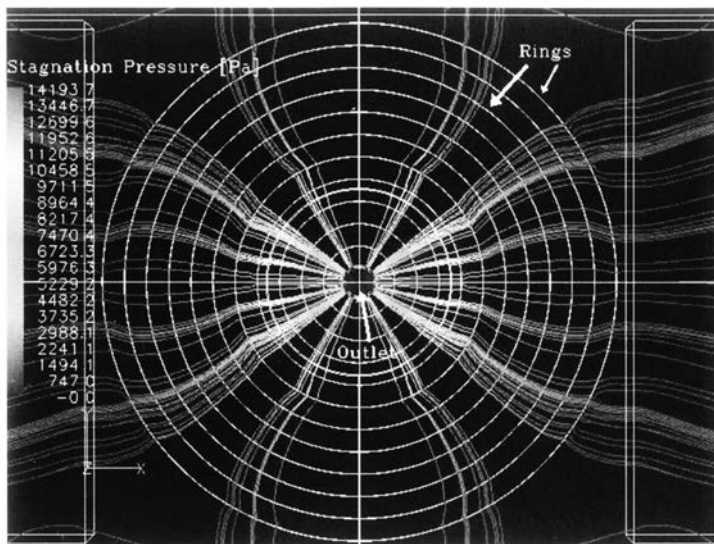

Fig. 11. Top view showing pathlines of selected particles over the rings between the seat and boss plates for a gap of 2.7 mm and pressure drop of 2.4 psi. The path of particles released at the inlet are colored by the local fluid stagnation pressure. The color bar on the left shows the pressure values.
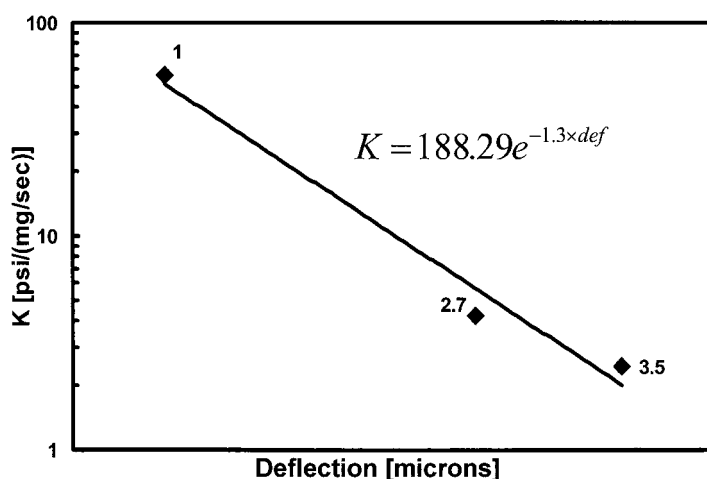
$$K = 188.29e^{-1.3 \times def}$$

Fig. 12. Pressure drop coefficient versus deflection. The slopes of the pressure drop versus flowrate data were computed and they exhibit an exponential dependence on the deflection. Given the uncertainty in the value of gap inherent in the system, the discrepancies between the measurements and computational predictions are attributed to such errors in value of gap.

of a perfect gas between two insulated, parallel disks flowing radially toward an outlet hole at the center of the bottom disk as shown in Fig. 13. The 4th order Runge-Kutta algorithm was utilized to integrate a system of nonlinear ordinary differential equations relating the various flow properties. The effect of friction was accounted for via utilization of a modified friction coefficient that depended on height and spacing between concentric rings and the flow Reynolds number.[22] The measured flow rate vs. displacement information for an imposed pressure[17] was used to establish the flow conditions at the inlet plane of the gap identified at radial location r_i in Fig. 13. The predictions were performed for gaps of 11, 12, 13, 14 and 15 microns under operating conditions of 100, 200 and 300 psi. The variation of the Mach number (M^+) is shown in Fig. 14 for an operating pressure of 100 psi. The superscript + is used to denote the local quantity made dimensionless by the value of that variable at the inlet to the gap, so the dimensionless variable starts at 1. The operating Mach numbers of the current radial flow cases were subsonic. Therefore, a gradual increase of the Mach number in the flow direction due to the action of friction is expected.[23] Due to the negligible change in the gas temperature,[21] dimensionless velocity exhibited similar trends. The dramatic rise of the static pressure in the flow direction is shown in Fig. 15. The pressure rise is observed to be weakly affected by the initial conditions or the gap between the two disks. Also shown on this figure is the pressure variation of an ideal incompressible fluid moving radially inward. In contrast to the pressure rise trends predicted by the compressible model, the ideal incompressible model predicts that the pressure will decrease in the flow direction. The numerical predictions of the total pressure drop through the passageway are summarized in Table 2. These compressible flow predictions are also compared to the total pressure drop relation for
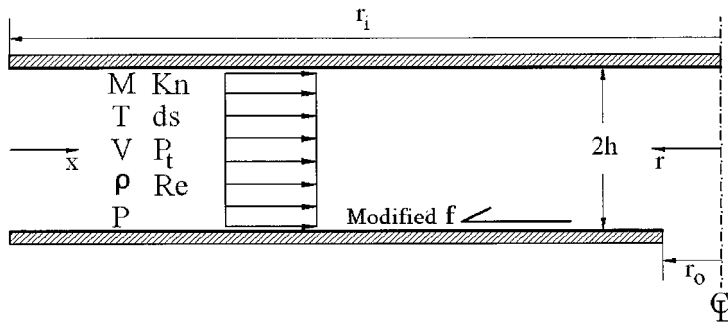
Fig. 13. Geometry of the 1-D axisymmetric radial model. The flow properties vary inward in the positive x-direction (opposite to the radial coordinate, r) as the gas gets closer to the outlet opening tube with the radius of r_o.
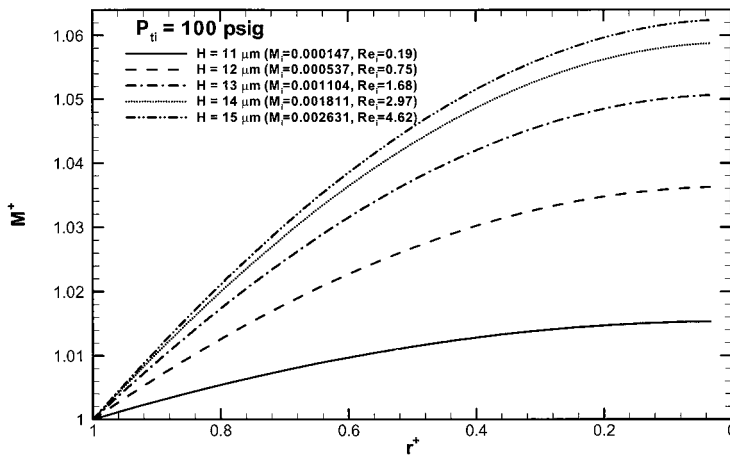

Fig. 14. Variation of the dimensionless Mach number for an inlet pressure of 100 psi. The dimensionless Mach number is obtained by dividing the local Mach number by its value at the inlet to the gap ($r^+ = 1$). The dimensionless radial coordinate ($r^+ = r/r_i$) extends from the inlet of the gap at $r^+ = 1$ to the location of the outlet tube. The continuous rise of the Mach number is due to friction.

incompressible Stokes flow.[21] It is clear that the total pressure drop for Stokes (Re<<1) incompressible flow is consistently lower than the predictions of the radial model that accounts for the compressibility effect. For an imposed total pressure at the inlet station (P_{ti} = constant), both approaches indicate that as the spacing is changed from 11 to 15 μm, the incurred total pressure drop is observed to rise with the mass flowrate. The percentage difference between the predictions and Stokes relation diminishes as the spacing is raised. This is expected since the effect of the ring becomes more negligible as the two disks move apart and the Stokes model becomes more realistic.
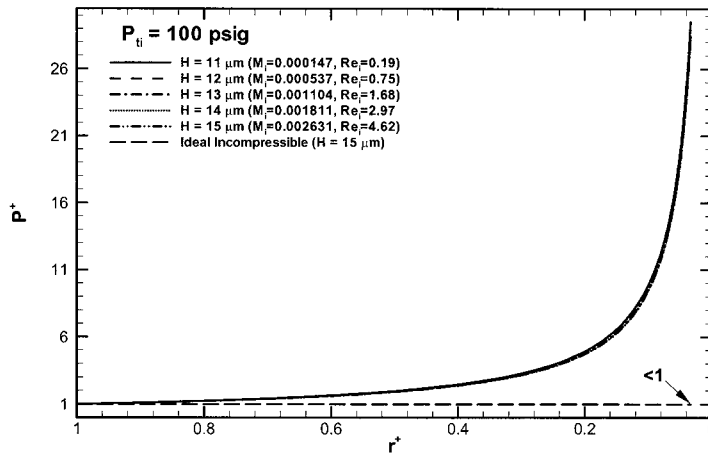
Fig. 15. Variation of the dimensionless static pressure for an inlet pressure of 100 psi. The dimensionless static pressure is obtained by dividing the local static pressure by its value at the inlet to the gap ($r^+ = 1$). Also shown is the prediction based on an ideal (frictionless) incompressible model.

Table 2
Total pressure drop ($\Delta P_t^+ = P_{ti} - P_{t0}$) for the radial flow model compared to the incompressible Stokes model.

P_{ti} (psig)	H (μm)	Q_{actual} (m^3/min)	Mass Flowrate (mg/min)	Numerical ΔP_t (kPa)	Stokes ΔP_t (kPa)
	11	1.844E-06	2.1131	11.9311	2.3356
	12	7.350E-06	8.4209	27.6364	7.1983
100	13	1.636E-05	18.7456	38.1025	12.6963
	14	2.891E-05	33.1248	43.8836	18.1660
	15	4.499E-05	51.5460	46.4365	23.3444
	11	1.583E-06	3.5625	9.5476	2.0067
	12	8.390E-06	18.8764	29.3631	8.2697
200	13	2.047E-05	46.0634	44.4654	16.1761
	14	3.783E-05	85.1237	53.8081	24.6497
	15	6.047E-05	136.0571	58.8977	33.3647
	11	1.225E-06	3.9854	7.2085	1.5531
	12	6.797E-06	22.1099	23.1575	6.7128
300	13	1.677E-05	54.5612	35.4285	13.3260
	14	3.115E-05	101.3395	43.1155	20.5233
	15	4.994E-05	162.4447	47.4225	28.0650

6.　Conclusions

We have successfully demonstrated piezoelectrically-actuated, gas- and liquid-compatible silicon microvalves. The microvalve incorporates a custom-designed piezoelectric stack actuator to provide the actuation forces necessary for high-pressure operation. A hard seating configuration using a series of narrow concentric seating rings contributes to the enhanced leak-tight microvalve operation. Reliable and reproducible microvalve operation has been demonstrated. The microvalve is capable of proportional flow control of liquid propellant for integrated micropropulsion applications. Computational modeling tools have been utilized and/or developed for prediction of the flow-related quantities within both liquid and gas microvalves. The dominant trends showing further degradation of the pressure for higher flow rates were predicted by these models. Potential applications for this microvalve technology include low impulse-bit thruster modules for use in very small spacecraft as well as for providing precise attitude control functions for larger spacecraft.

References

1　M. J. Zdeblick, R. Anderson, J. Jankowski, B. Kline-Schoder, L. Christel, R. Miles, and W. Weber: Solid-State Sensor and Actuator Workshop (Hilton Head, SC, 1994) p. 251.
2　P. W. Barth: Transducers '95 (Stockholm, 1995) p.276.
3　X. Yang, C. Grosjean, Y. C. Tai, and C. M. Ho: MEMS '97 (Nagoya, 1997).
4　H. Jerman: Solid State Sensor and Actuator Workshop (Hilton Head, SC, 1990) p. 67.
5　J. Franz, H. Baumann, and H. Trah: Transducers'95 (Stockholm, 1995).
6　C. Ray, C. Sloan, D. Johnson, J. Busch, and B. Petty: Mat. Res. Soc. Symp. Proc. **276** (1992) 161.
7　J. Busch, and D. Johnson: Proc. IEEE (1990) p. 40.
8　M. Huff, J. Gilbert, and M. Schmidt: Transducers'93 *(*Yokohama, 1993).
9　M. Huff and M. Schmidt: Solid State Sensor and Actuator Workshop *(*Hilton Head, SC, 1992) p.194.
10　M. Shikida, K. Sato, S. Tanaka, Y. Kawamura and Y. Fujisaki: Transducers '93 *(*Yokohama, 1993.
11　T. Ohnstein, T. Fukiura, J. Ridley and U. Bonne: Proc. IEEE (1990) 95.

12   S. Kluge, G. Klink and P. Woias: American Laboratory (19980) p. 17.
13   M. Capanu, J. G. Boyd and P. J. Hesketh: Journal of Microelectromechanical Systems **9** (2000)181.
14   H. Kawada, H. Yoshida, M. Kamakura, K. Yoshida, M. Saitou, M., Kawahito and S. Tomonari, Transducer'03 (2003) p. 1935.
15   S. Messner, J. Schaible, J. Vollmer, H. Sandmaier, and R. Zengerle: IEEE MEMS '03 (2003) p. 88.
16   S. Kluge, G. Neumayer, U. Schaber, M. Wackerle, M. Maichl, P. Post, M. Weinmann and R. Wanner: Transducers' 01 (2002) p. 924.
17   E. H. Yang, C. S. Lee, J. Mueller and T. George: Journal of Microelectromechanical Systems **13** (2004).
18   C. Lee, E. H. Yang, S. M. Saeidi and J. M. Khodadadi: Journal of Microelectromechanical Systems **15** (2006) 686.
19   S. V. Patankar: Numerical Heat Transfer and Fluid Flow (McGraw-Hill, NY, 1980).
20   S. M. Saeidi: Ph.D. Thesis (Auburn University, 2005).
21   C. A. Johnson: MS Thesis (Auburn University, 2005).
22   C.-D. Luy, C.-H. Cheng and W.-H. Huang: Applied Energy **39** *(*1991) 127.
23   J. E. A. John: Gas Dynamics (Prentice-Hall Inc., NJ, 1984).